

Article

Seismic Performance Assessment of Wide Pile-Supported Wharf Considering Soil Slope and Waveform Duration

Christino Boyke ^{1,*}  and Takashi Nagao ² 

¹ Department of Marine Transportation Engineering, Faculty of Marine Technology, Institut Teknologi Sepuluh Nopember, Surabaya 60111, Indonesia

² Research Center for Urban Safety and Security, Kobe University, Kobe City 657-8501, Japan; nagao@people.kobe-u.ac.jp

* Correspondence: c.boyke@seatrans.its.ac.id

Abstract: Pile-supported wharf (PSW) is one of the primary port structures and is often damaged by earthquakes. To mitigate the risk of seismic damage to a PSW, its seismic performance should be thoroughly assessed. This study aimed to examine the impact of ground displacement on the seismic performance of PSW with a mild soil slope. We performed soil-structure system finite element analysis targeting a wide PSW. The analysis is divided into two scenarios. In the first scenario, the PSW was modeled without regard for the soil slope, whereas the second scenario considered the soil slope. Two waveforms that matched the target spectral acceleration were used to study the effects of the waveform duration on the seismic response of PSW. The analysis results revealed substantial influences of soil slope displacement as well as differences in waveforms on PSW's seismic performance.

Keywords: pile-supported wharf; seismic response; finite element analysis; ground displacement; residual displacement



Citation: Boyke, C.; Nagao, T.

Seismic Performance Assessment of Wide Pile-Supported Wharf Considering Soil Slope and Waveform Duration. *Appl. Sci.* **2022**, *12*, 7266. <https://doi.org/10.3390/app12147266>

Academic Editors: Linsheng Huo and Dongdong Chen

Received: 29 June 2022

Accepted: 17 July 2022

Published: 19 July 2022

Publisher's Note: MDPI stays neutral with regard to jurisdictional claims in published maps and institutional affiliations.



Copyright: © 2022 by the authors. Licensee MDPI, Basel, Switzerland. This article is an open access article distributed under the terms and conditions of the Creative Commons Attribution (CC BY) license (<https://creativecommons.org/licenses/by/4.0/>).

1. Introduction

Pile-supported wharf (PSW) is one of the primary port structures that facilitates the transfer of shiploads and ship berthing. A PSW typically comprises a deck, pile foundation, and supporting facilities such as trestle bridges. Many PSWs are located in seismically active areas and are susceptible to damage and loss of function. For example, the Loma Prieta earthquake in 1989 caused severe damage to the Port of Oakland, such as pile heads failure, settlement, and lateral spreading [1]. The Port de Port-au-Prince was severely damaged during the Haiti earthquake in 2010, when the PSW was significantly displaced toward the sea, submerging the gantry crane [2]. Such loss of PSW serviceability directly impacts the operation of the entire port infrastructure, resulting in significant economic losses. To mitigate the risk of seismic damage to a PSW, its seismic performance must be thoroughly assessed.

A PSW is comprised of two components: a frame structure and earth-retaining components. Since the ground displacement occurs in the earth-retaining component during an earthquake, it is necessary to properly carry out the seismic response analysis of PSWs considering this effect. The seismic performance of PSWs has been investigated in many previous studies. Soil-structure system finite element analysis (FEA) results for PSWs with a deck length of 31 m or less showed that ground displacement greatly affected the seismic safety of the piles [3–6]. For instance, Su et al. [3] performed a full three-dimensional soil-structure FEA on a 31 m-wide PSW with a soil slope ratio of 1:1.5 (vertical to horizontal) and showed the significant influence of soil slope deformation on the pile's seismic response. Torkamani et al. [4] analyzed a PSW's seismic performance using a two-dimensional (2D) finite-difference model subjected to eight ground motion records. The modeled PSW was 28 m-wide with a soil slope ratio of 1:2. The results showed that loose sand porosity

contributed most to the PSW's residual displacement variance, while the internal friction angle of loose sand contributed most to differential settlement. Hamrouni et al. [5] used 2D FEA to investigate the behavior of a PSW during the Loma Prieta earthquake in 1989. The results indicated that significant lateral ground displacement occurred in the upper portion of the embankment due to the liquefaction of loose sand and impacted the piles' displacement. Nagao and Lu [6] conducted a series of 2D FEA targeting a PSW and showed that the residual displacement of a PSW is mainly caused by the deformation of subsoil. The effect of soil displacement on PSWs could be more severe in PSWs that have been affected by corrosion [7,8].

Ground motion characteristics such as amplitude, frequency characteristic, and waveform duration have long been recognized as essential factors influencing structural response [9–11]. Of the three, amplitude and frequency characteristics are generally taken into consideration by spectral acceleration (SA), which the engineering society has commonly accepted as the primary basis for structural design and assessment. Conversely, waveform duration has received less attention, particularly in PSW's seismic assessment. Several studies, including Barbosa et al. [12], Ou et al. [13], Romney et al. [14], Mantawy and Anderson [15], and Chandramohan [16], have employed nonlinear dynamic analyses to assess the influence of the waveform duration, specifically on buildings and bridges. The broad agreement emerging from these studies is that while waveform duration has little effect on peak demands such as peak story drifts and peak member forces, it significantly affects cumulative damage metrics such as residual displacement and accumulated plastic strain.

Pushover analysis [17–19] is a widely used method to perform seismic performance assessment of a PSW. The performance point and fragility curves of a PSW can be evaluated by using pushover analysis. This analysis calculates a PSW's seismic performance with considerable accuracy when the PSW is located on a horizontally stratified ground; however, it cannot take into account the effect of ground deformation caused by an earthquake and waveform duration.

Considering the lack of research on ground displacement and waveform duration impact on the seismic performance of a PSW with a mild soil slope, we assessed the seismic performance of a wide PSW commonly used in Indonesia. The targeted PSW comprises a trestle bridge and a wharf, with a total width of 165 m. Since its width is large, the slope under the trestle bridge is mild, with a slope ratio of 1:5, and the effect of ground displacement is considered to be negligible in seismic design practice. Accordingly, analysis modeling of only the framed structural part has often been carried out [20–22], though the validity of this practice has not been confirmed.

This study aimed to provide a more comprehensive approach to the seismic performance assessment of wide PSWs. Our study employed a 2D soil-structure system FEA with/without considering a soil slope to investigate the effect of ground deformation on the wide PSW's seismic performance. In addition, two waveforms, of short and long duration, were used as motion inputs to study the effects of the waveform's duration on the seismic response of the PSW.

2. Methods

2.1. Target PSW

The target PSW is a rigid-frame structure with a steel pipe pile foundation and reinforced concrete deck built in Indonesia. Because of the mild slope of the seabed, the PSW was built far from the coast to meet the required water depth for container ships; therefore, a trestle bridge is needed to connect it to the land.

The target PSW and ground configurations are depicted in Figure 1. The dimension of the wharf is 80 m × 300 m, and it is connected to the trestle bridge of 85 m × 13 m and the causeway of 60 m wide. The crown height of the wharf is +4.00 m low water spring (LWS), and the deck is supported by 15 rows of vertical steel pipe piles with diameters (Ø) of 1100 and 1200 mm that rest on −13 m LWS seabed. The trestle bridge is composed of

a reinforced concrete deck, and 17 rows of Ø1000 mm steel pipe piles that sit on a mild soil slope with a slope ratio of 1:5. The trestle and wharf were combined and responded integrally against earthquakes.

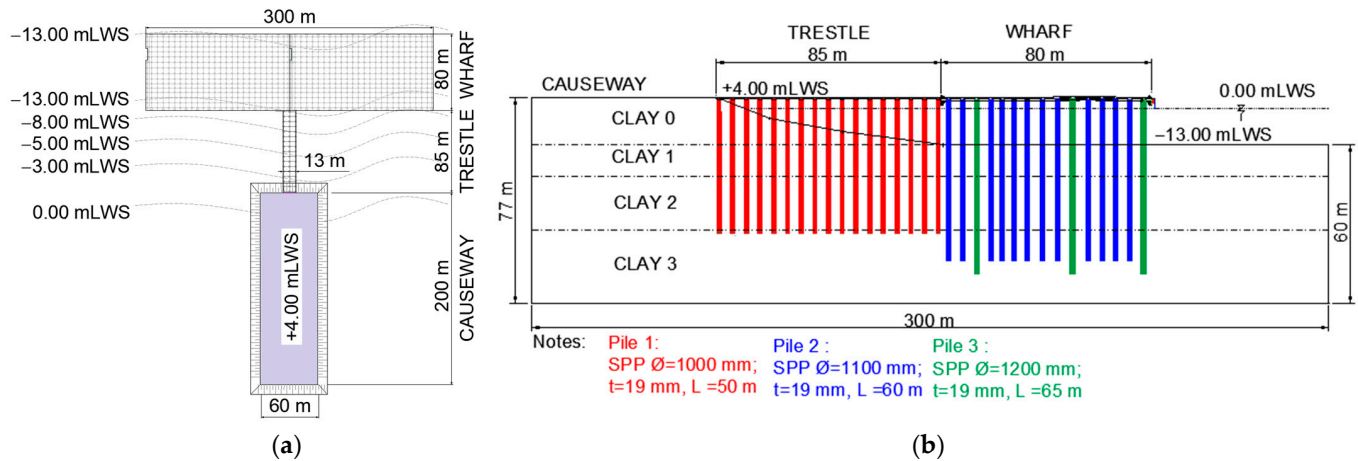


Figure 1. PSW configuration. (a) plan view; (b) side view.

Table 1 shows the soil properties obtained from a soil investigation. The ground consists of four silty clay layers, where Clay 0 is a soft clay at the landside ground surface, and Clay 3 is a stiff ground where the pile's bottom end rests. Each soil layer's shear wave velocity (V_s) was calculated using the correlation equation with the N-value observed from the standard penetration test (N-SPT) proposed by Imai and Tonouchi [23]. The average shear wave velocity of the top 30 m (V_{s30}) of this site was 174.5 m/s; it falls into site class E (soft ground) according to the Indonesian seismic code SNI 1726 2019 [24]. The natural frequency of the ground was determined to be 0.94 Hz.

Table 1. Soil properties.

Layer Code	N-SPT	Layer Thickness (m)	Soil Type	Specific Gravity (GS)	Water Content (W_n (%))	Unit Weight (γ_n (kN/m ³))	Void Ratio (e)	Liquid Limit (LL (%))	Plastic Limit (PL (%))	Shear Wave Velocity (V_s (m/s))
Clay 0	5–8	17	Soft Clay	2.60	29.67	13.34	1.44	49.5	21.8	162.1
Clay 1	10	12	Medium Stiff Silty Clay	2.61	33.67	14.12	1.43	52.6	24	197.7
Clay 2	11–16	20	Medium Stiff Silty Clay	2.62	41.84	14.32	1.41	52.7	23	210
Clay 3	30–60	28	Very Stiff Silty Clay	2.63	38.08	14.51	1.4	52.5	22	332

2.2. Finite Element Modeling

PLAXIS 2D [25] was used to create a 2D FEA model. PSW models were constructed using 15 nodal-point triangular elements and analyzed as plane strain models. This analysis utilized two sequential loading phases to represent the actual state of the structure: static (i.e., only accounting for PSW and soil self-weight) and earthquake phase. In the static phase, the boundary conditions for side boundaries were set as normally fixed, while that for the bottom boundary was endowed with fully fixed. Regarding the earthquake phase, free-field and compliant base boundaries were applied to the side boundaries and bottom boundary, respectively [26]. The fine mesh option was selected when choosing the mesh coarseness to transmit ground motions in a high-frequency range.

The hardening soil small-strain (HSS) model was applied to account for nonlinear soil behavior. The HSS model is a modification of the hardening soil model that accounts for the increased stiffness of soils at small strains [26], which is described by two additional material parameters of G_0^{ref} (the small-strain shear modulus) and $\gamma^{0.7}$ (the shear strain level at which the small-strain shear modulus has decreased to approximately 70% of its initial

value) [27]. In this study, the drainage condition was modeled as undrained- A, which provides better numerical simulation performance in the seismic case than other options in PLAXIS [26]. Plate elements were used to model the deck. An embedded beam row element was applied to model the piles. This feature allows for the 2D modeling of piles with a particular spacing in out-of-plane direction and has been validated by comparisons with three-dimensional FEA models and measurements from actual tests [28–30].

The 2D FEA was divided into two scenarios to allow for a more accurate comparison of PSW seismic performance between the two modeling approaches. In Scenario 1, the PSW was modeled without regard to the seabed's slope and displacement (Figure 2a). Scenario 2 took the seabed slope and its displacement into account (Figure 2b). Each scenario was subjected to two distinct waveforms of varying durations as the input motion. Thus, four analysis cases were conducted in this study.

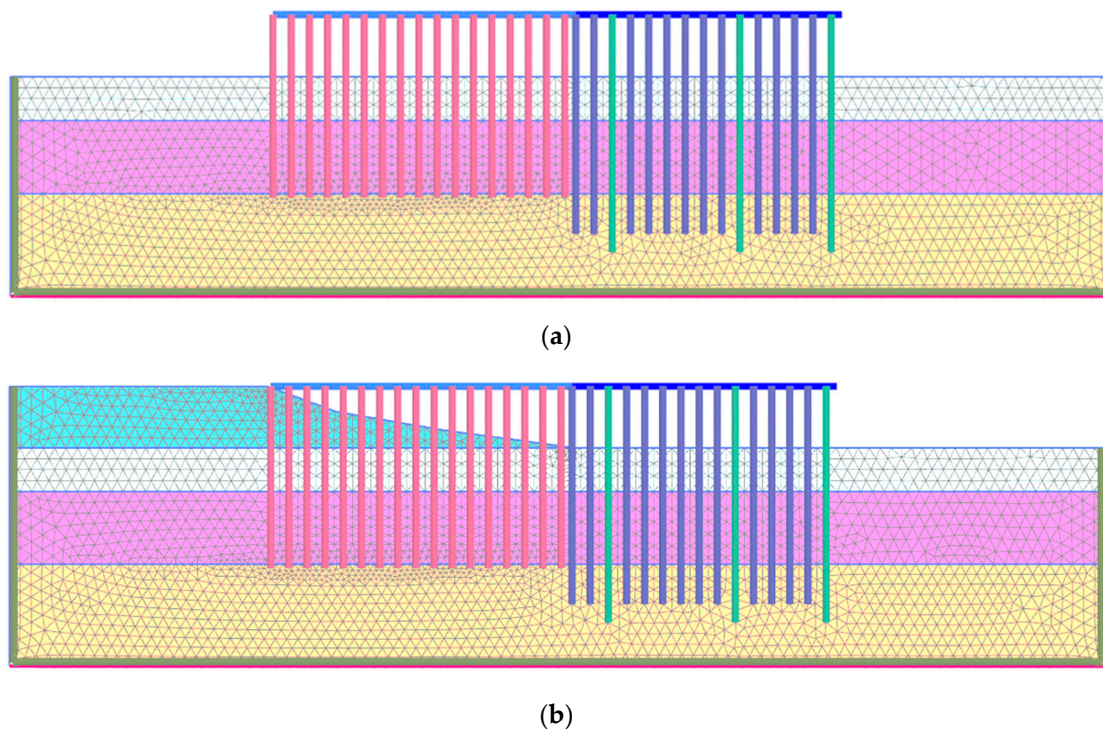


Figure 2. Finite element model. (a) Scenario 1; (b) Scenario 2.

Table 2 describes the soil parameters used in the HSS model. The compression (C_c) and swelling (C_s) indices were calculated based on Bowles [31] (Equations (1) and (2)). The initial void ratio (e_{init}) was evaluated as a function of Wn [32] (Equation (3)). The $\gamma^{0.7}$ was calculated using Equation (4) based on its correlation with PL [33]. The G_0^{ref} was estimated in correlation with the N-SPT value based on Imai and Tonouchi [23] (Equation (5)).

$$C_c = 0.007 (LL - 7) \quad (1)$$

$$C_s = 1/5 C_c \quad (2)$$

$$e_{init} = 0.0197 Wn + 0.2143 \quad (3)$$

$$\gamma^{0.7} = 1.10^{-4} + 5.10^{-4} PL \quad (4)$$

$$G_0^{ref} = 14.12 N^{0.68} \text{ (MPa)} \quad (5)$$

Table 2. Input parameters for HSS model.

Parameter	Unit	Clay 0	Clay 1	Clay 2	Clay 3
γ_{sat}	kN/m ³	16.24	16.31	16.40	16.47
γ_{unsat}	kN/m ³	13.35	14.11	14.29	14.53
C_c		0.0297	0.0319	0.0320	0.0319
C_s		0.00595	0.00638	0.00640	0.00637
e_{init}		0.77	0.88	1.10	1.00
C'_{ref}	kN/m ²	2.5	5	10	20
ϕ'		23	25	27	35
Ψ		0	0	0	0
$\gamma^{0.7}$		0.00021	0.00022	0.00022	0.00021
G_0^{ref}	kN/m ²	42,206.6	67,620.9	93,085.6	228,677.6

Note: γ_{sat} is saturated soil unit weight, γ_{unsat} is unsaturated soil unit weight, C'_{ref} is effective cohesion, ϕ' is effective internal friction angle, and Ψ is dilatancy angle.

Table 3 describes the pile parameters used in the embedded beam row element. The pile was modeled as an elastoplastic circular tube beam and divided into three pile types, namely, pile 1 for trestle foundation and piles 2 and 3 for wharf foundation. The piles had a yield strength of 2.4×10^5 kN/m² and a Young's modulus of 2.0×10^8 kN/m². The out-of-plane pile spacing was 6 m. Lateral resistance (T_{lat}) was calculated using Equation (6), using the correlation between undrained cohesion (Cu) and \emptyset [34]. Axial (F_{max}) and skin (T_{skin}) resistance were calculated based on Décourt [35]. T_{skin} in Equation (7) was calculated considering pile base friction coefficient (β) [36] average N-SPT value at embedded pile depth (NS), pile cross-sectional area (A_p), and embedded pile depth (L). F_{max} (Equation (8)) was calculated considering pile base coefficient (α) [36] average N-SPT value in between $4\emptyset$ below and $4\emptyset$ above pile tip (NP), characteristic soil coefficient (K) [36], and A_p . In this model, T_{lat} and T_{skin} values were set to linearly increase from the smallest at the pile head to the largest at the pile tip.

$$T_{lat} = 9 Cu \emptyset \quad (6)$$

$$T_{skin} = \beta (NS/3 + 1) A_p L \quad (7)$$

$$F_{max} = \alpha NP K A_p \quad (8)$$

Table 3. Input parameters for embedded beam row elements.

Parameter	Unit	Pile 1	Pile 2	Pile 3
\emptyset	m	1	1.1	1.2
t	m	0.019	0.019	0.019
A_p	m ²	0.585	0.651	0.717
I	m ⁴	0.00705	0.0107	0.0129
M_p	kN·m	4392	5522	6583
N_p	kN	140,544	156,000	170,400
$T_{skin,start}$	kN/m	130	149	162
$T_{skin,end}$	kN/m	440	500	577
F_{max}	kN	4780	5440	6020
$T_{lat,start}$	kN/m	108	118	130
$T_{lat,end}$	kN/m	2340	2673	2916
Z	m ³	1.83×10^{-2}	2.30×10^{-2}	2.74×10^{-2}

Note: t is thickness of pile, I is moment of inertia, M_p is plastic bending moment, N_p is plastic axial force, and Z is section modulus.

The reinforced concrete decks are modeled as plate elements, and their material properties are outlined in Table 4. The elements were modeled as an elastoplastic-isotropic material with a compressive strength of 35 MPa, a Poisson's ratio of 0.2, and a Young's modulus of 2.7×10^7 kN/m². The wharf deck had a larger dimension and capacity than the trestle deck due to the greater load that a wharf must withstand. For the wharf, the live

load per unit width and depth was set at 20 kN/m/m, while for the trestle, it was set at 10 kN/m/m.

Table 4. Input parameters for plates.

Parameter	Unit	Wharf	Trestle
b	m	1	1
h	m	1	0.7
A	m	1	0.7
I	m ⁴	0.0833	0.0200
M_p	kN·m	3503.5	1282.38
N_p	kN	16,721	8543

Note: b is width, h is height, and A is profile area.

2.3. Input Waveforms

To investigate the effect of waveform duration on the seismic response of PSW, this study employed two distinct waveforms: short-duration waveform (SDW) and long-duration waveform (LDW). We used two reference waveforms observed in Indonesia [37], as shown in Figure 3. These waveforms were modified to match the target SA on Indonesian site class E [37] (Figure 4). The following procedures were implemented based on the observation that the frequency characteristics of the Fourier spectrum of a waveform and SA are similar [38]. First, the Fourier spectrum and SA of each reference waveform were calculated. The ratio of the target SA to the calculated SA at each frequency was then calculated. Next, the Fourier spectrum was multiplied by the ratio. The spectrum was then inverse Fourier transformed to obtain time history data. SA was then calculated and compared with the target SA. The previous steps were repeated until a waveform that best fit the target SA was obtained. It should be noted that the procedure conserved Fourier phase spectra of the reference waveforms. The comparison between the target SA and the obtained SA is depicted in Figure 4. The obtained SA matches the value of the target SA, particularly in the period range of 1 s or longer. Figure 5 illustrates the waveforms obtained from this procedure. The obtained waveforms have similar envelopes to the reference waveforms.

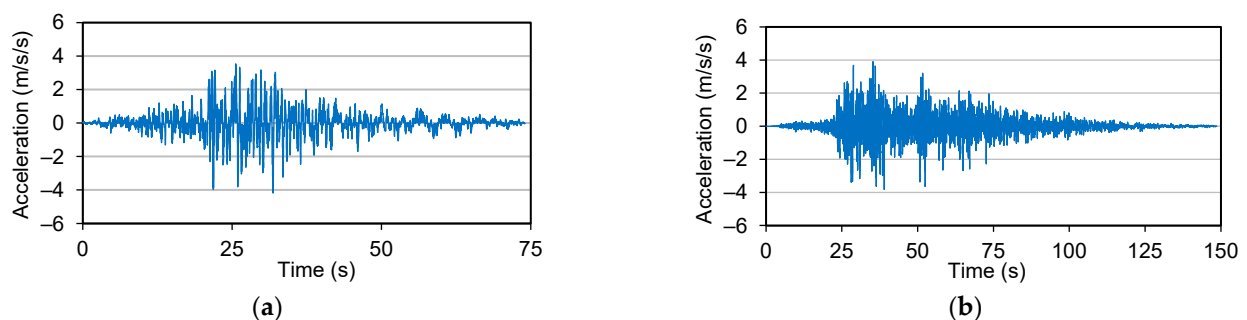


Figure 3. Reference waveforms. (a) SDW; (b) LDW.

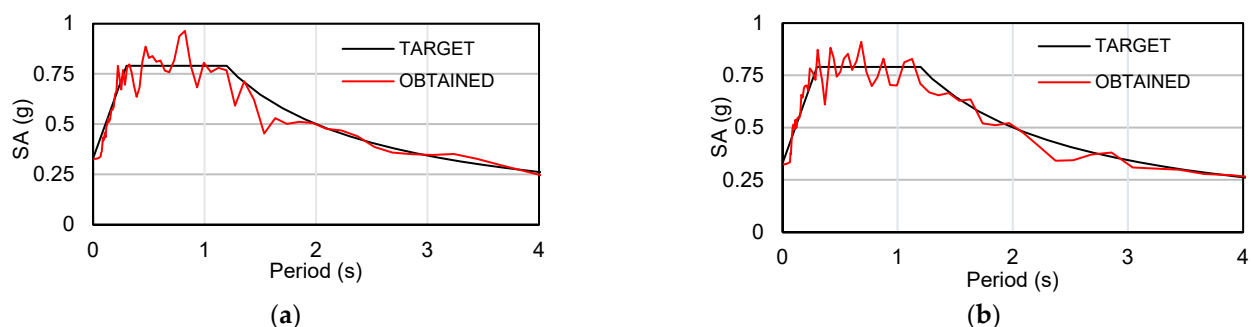


Figure 4. Target and obtained SAs. (a) SDW; (b) LDW.

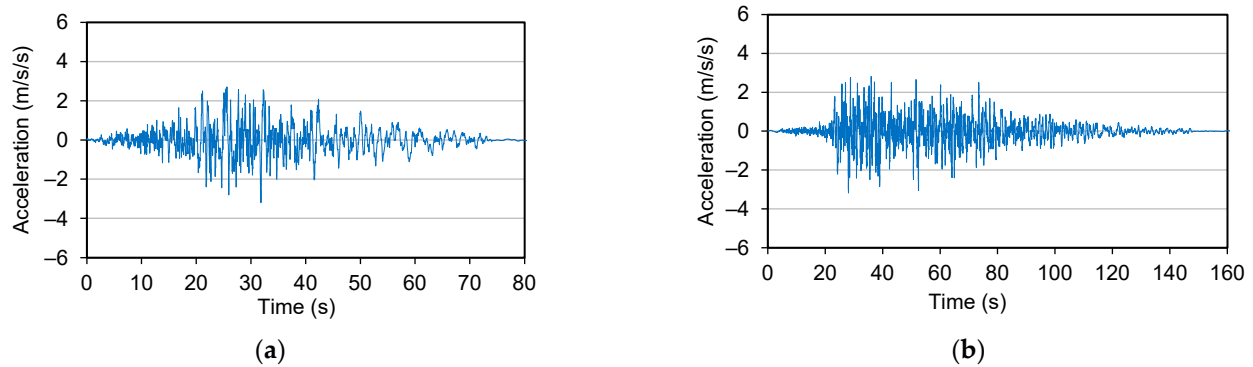


Figure 5. Obtained waveforms. (a) SDW; (b) LDW.

The obtained waveforms were the ones at the ground surface. To obtain input ground motions for FEA, a frequency domain seismic response analysis considering nonlinear soil characteristics was performed, and the incident waveforms at the bedrock were evaluated (deconvolution). For the shear modulus and the damping coefficient dependencies on the shear strain, we referred to Vucetic and Dobry [39]. Figure 6 illustrates the incident waveforms at the bedrock. The maximum acceleration at the bedrock was smaller than that at the surface. The peak acceleration of the SDW was 1.43 m/s/s at bedrock and 3.17 m/s/s at the surface. As for the LDW, the peak acceleration was 1.58 m/s/s at bedrock and 3.20 m/s/s at the surface.

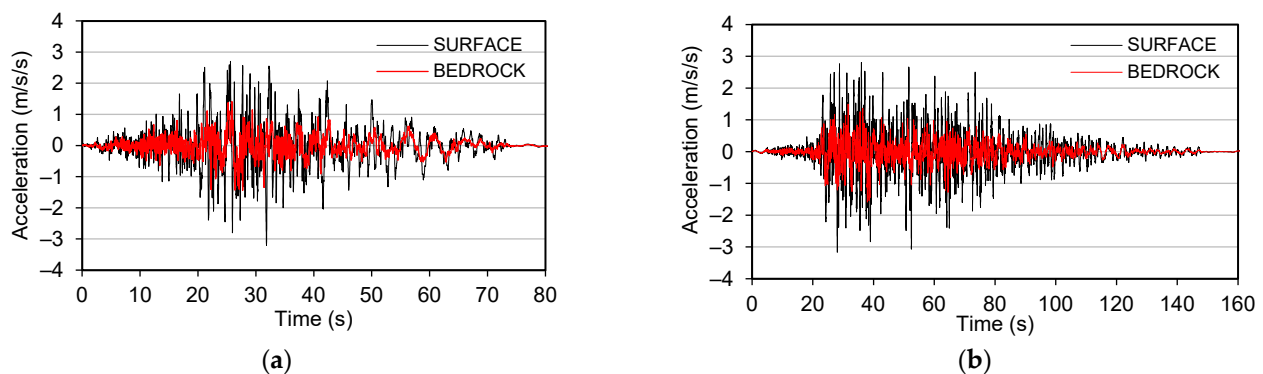


Figure 6. Input waveforms. (a) SDW; (b) LDW.

3. Results and Discussion

3.1. PSW Response

Figure 7 illustrates the horizontal acceleration time history at the PSW deck's top right (seaside) end in Scenario 1. The LDW produced a maximum acceleration of 0.8 g, more significant than the SDW at 0.55 g. The PSW and ground surface Fourier spectra in Scenario 1 are depicted in Figure 8. The Fourier spectra were smoothed by a log-triangle smoother [40]. The PSW and the ground surface showed different frequency characteristics; the predominant frequency of the PSW was 0.85 Hz, whereas that of the ground surface was 0.65 Hz. Therefore, the resonance effect was not significant.

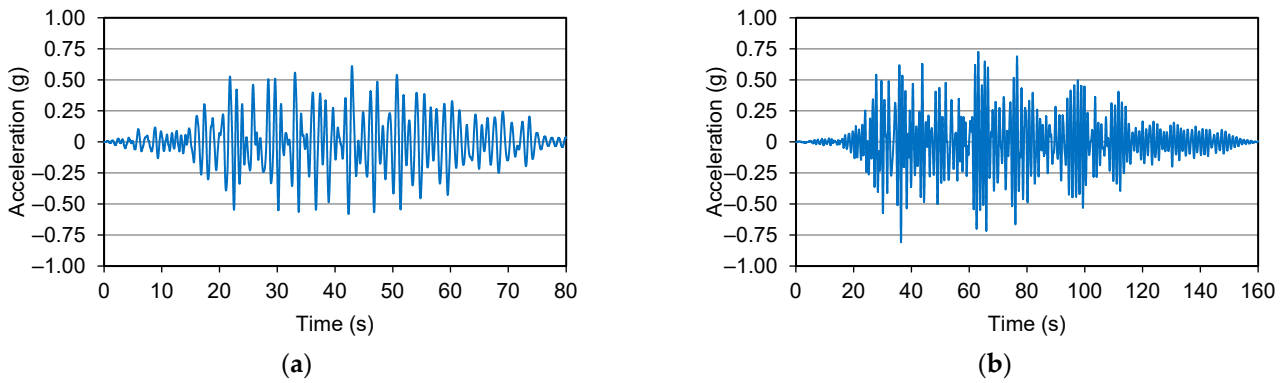


Figure 7. PSW time histories in Scenario 1. (a) SDW; (b) LDW.

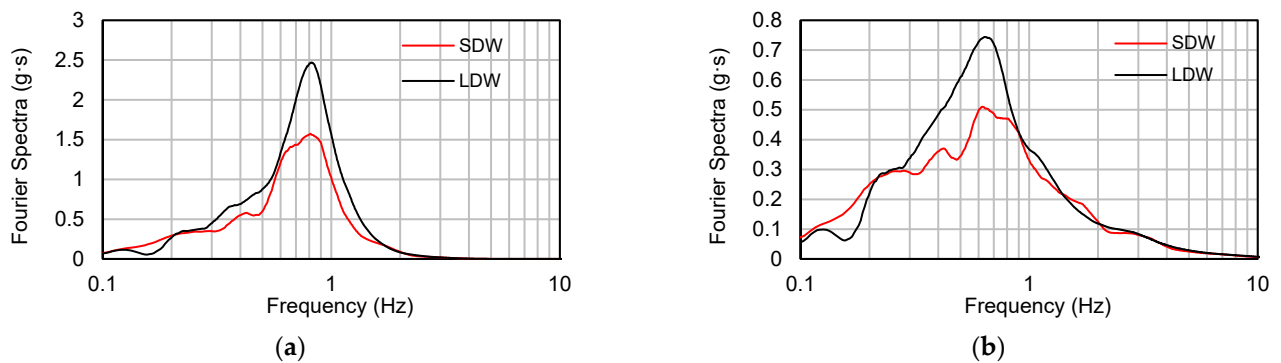


Figure 8. Fourier spectra in Scenario 1. (a) PSW; (b) ground surface.

The acceleration time history of the PSW in Scenario 2 is depicted in Figure 9. The LDW produced a maximum acceleration of 0.65 g, larger than the 0.55 g produced by the SDW. Figure 10 illustrates the PSW and landside’s ground surface Fourier spectra in Scenario 2. The PSW and the ground showed different frequency characteristics. The predominant frequency was 1.15 Hz for the PSW and 0.85 Hz for the ground surface. The natural period of the PSW in Scenario 2 was shorter than that in Scenario 1. This is because the pile’s free length in the slope part in Scenario 2 was shorter than in Scenario 1. Figures 8a and 10a illustrate that the Fourier spectra maxima of the PSW with the LDW were more significant than that with the SDW. The difference results from the different phase characteristics of the SDW and LDW.

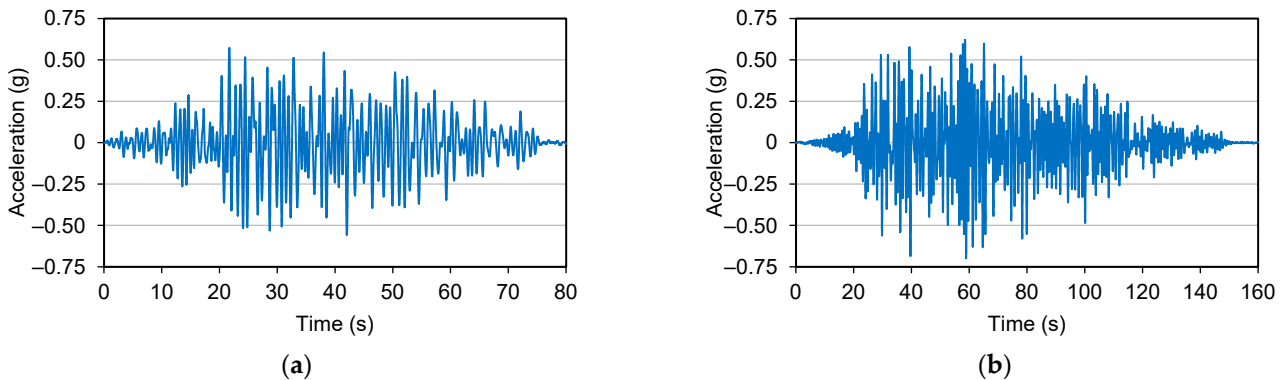


Figure 9. PSW time histories in Scenario 2. (a) SDW; (b) LDW.

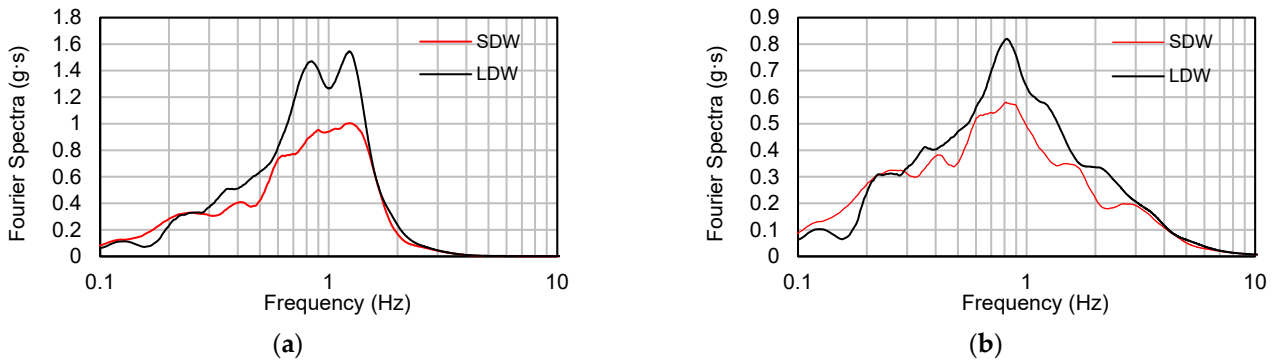


Figure 10. Fourier spectra in Scenario 2. (a) PSW; (b) ground surface.

3.2. PSW Horizontal Displacement

Figure 11 shows the PSW’s horizontal displacement time history in Scenarios 1 and 2 due to the SDW measured at the wharf deck’s top right (seaside) end. Here, seaward displacement is defined as positive. Scenario 1 produced a maximum displacement of 0.55 m, smaller than the 0.95 m in Scenario 2. Regarding the PSW’s residual displacement, it was 0.1 m in Scenario 1 and 0.6 m in Scenario 2. This difference is because Scenario 2 considered the soil slope’s residual displacement while Scenario 1 did not. The horizontal residual ground displacement contour map is illustrated in Figure 12. In Scenario 1, the residual ground displacement around the PSW was small, around 0.4–0.1 m. On the contrary, the residual ground displacement in Scenario 2 was large, around 1.2–0.5 m.

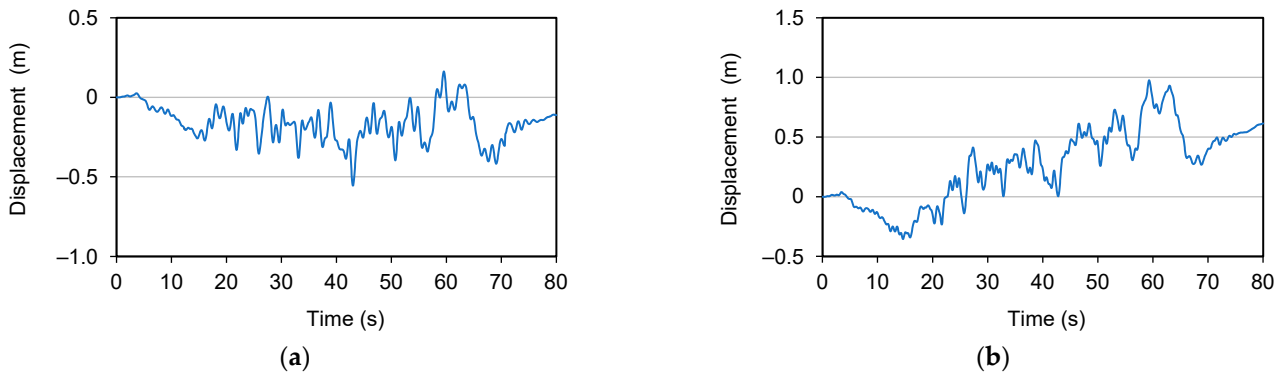


Figure 11. PSW horizontal displacement due to the SDW. (a) Scenario 1; (b) Scenario 2.

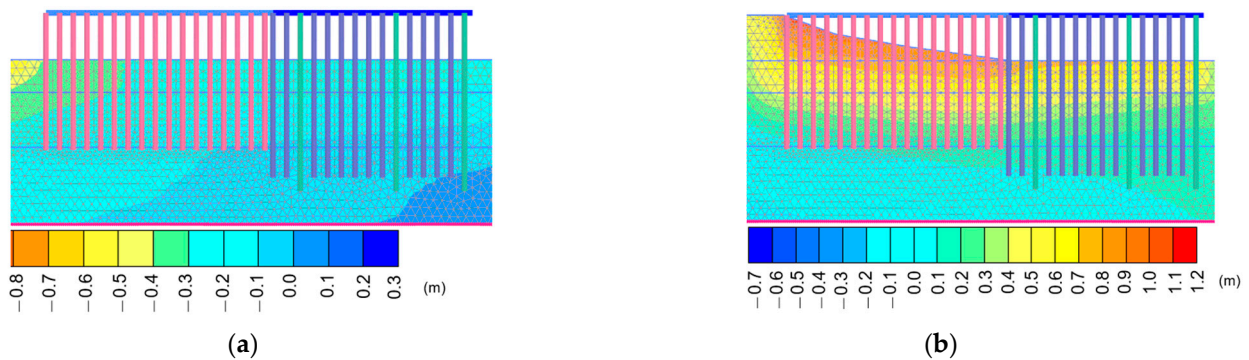


Figure 12. Horizontal residual ground displacement due to the SDW. (a) Scenario 1; (b) Scenario 2.

Figure 13 depicts the PSW’s horizontal displacement time history caused by the LDW in Scenarios 1 and 2. Scenario 1 had a maximum displacement of 0.85 m, less than the 1.35 m in Scenario 2. The residual displacement in Scenario 1 was 0.15 m, whereas that in Scenario 2 was 0.95 m. Figure 14 illustrates the horizontal residual ground displacement

contour map by the LDW. In Scenario 1, the residual ground displacement around the PSW was small, between 0.5 and 0.1 m. Conversely, the residual ground displacement in Scenario 2 was large, ranging from 2.0 to 0.8 m. The large PSW's displacement in Scenario 2 was due to the consideration of large ground displacement at the soil slope, which was neglected in Scenario 1. The LDW left a larger residual PSW displacement than the SDW. It should be noted that the LDW did not lead to large residual displacement because of the large number of shaking repetitions. Comparison of the results by the SDW and LDW of Scenario 2 shows that the displacement after 70 s almost coincides with the residual displacement, and no remarkable increase in the displacement occurred after 70 s by the LDW. The larger residual displacement by the LDW was caused by the phase characteristics of the LDW. Various waveforms can be realized that correspond to the target SA; therefore, it is recommended to consider waveforms having various phase characteristics in seismic design practice.

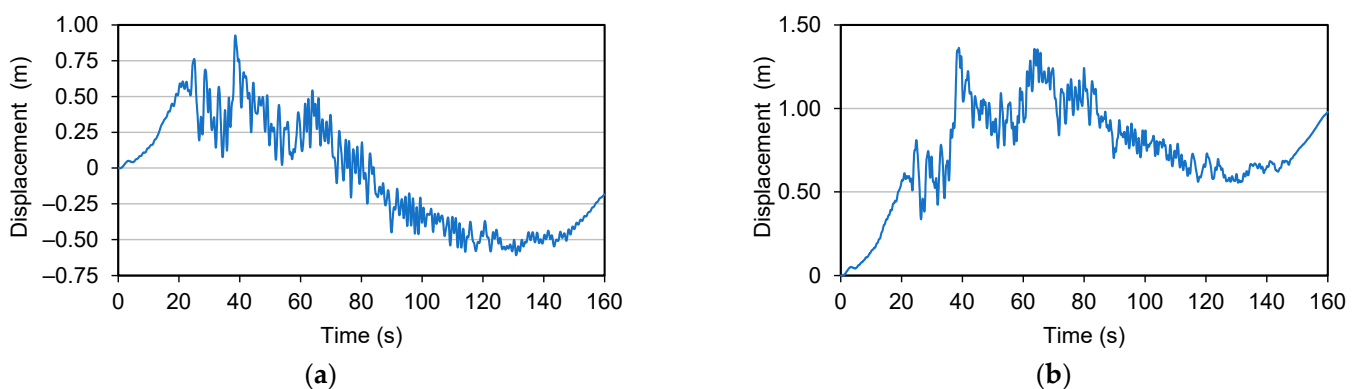


Figure 13. PSW horizontal displacement due to the LDW. (a) Scenario 1; (b) Scenario 2.

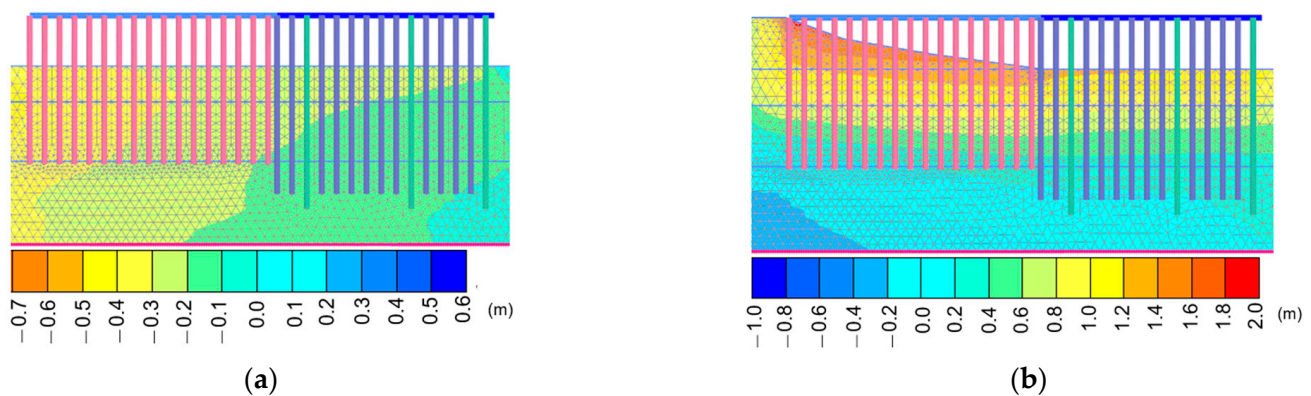


Figure 14. Horizontal residual ground displacement due to the LDW. (a) Scenario 1; (b) Scenario 2.

3.3. Bending Moment of Piles

Figures 15–20 illustrate the bending moment distributions of the piles due to the SDW and LDW, respectively. The distributions are the snapshots when the bending moment of each pile becomes maximum at a certain point in the pile. The piles are numbered sequentially from the left (smallest number) to the right (largest number) side. The Ø1000, Ø1100, and Ø1200 mm piles are labeled P1–P17, P1A–P12A, and P1B–P3B, respectively.

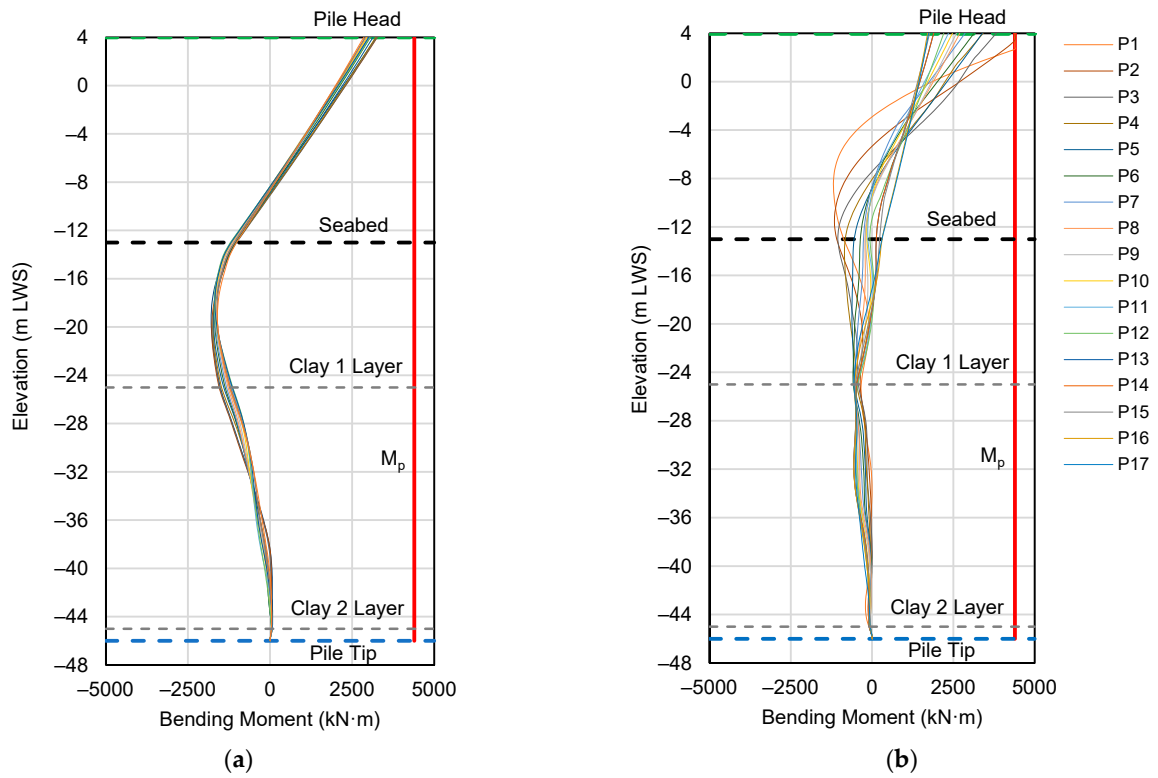


Figure 15. Bending moment distribution of Ø1000 mm pile due to the SDW. (a) Scenario 1; (b) Scenario 2.

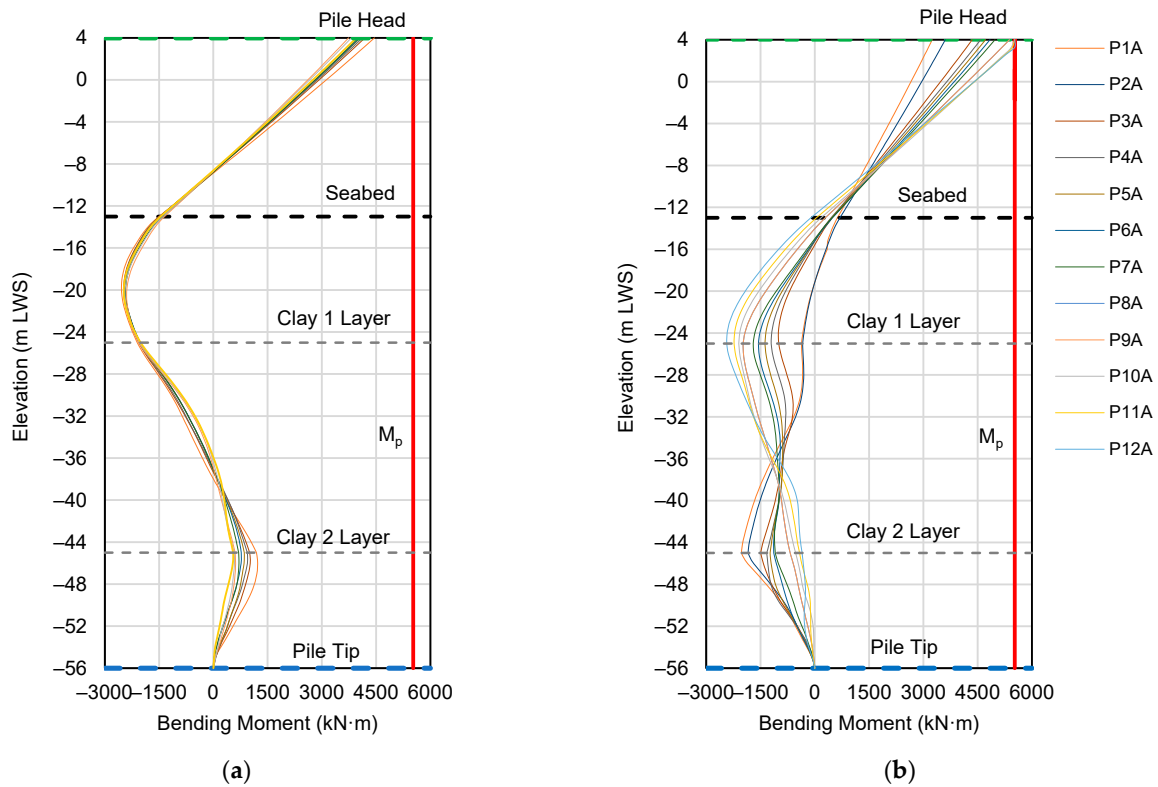


Figure 16. Bending moment distribution of Ø1100 mm pile due to the SDW. (a) Scenario 1; (b) Scenario 2.

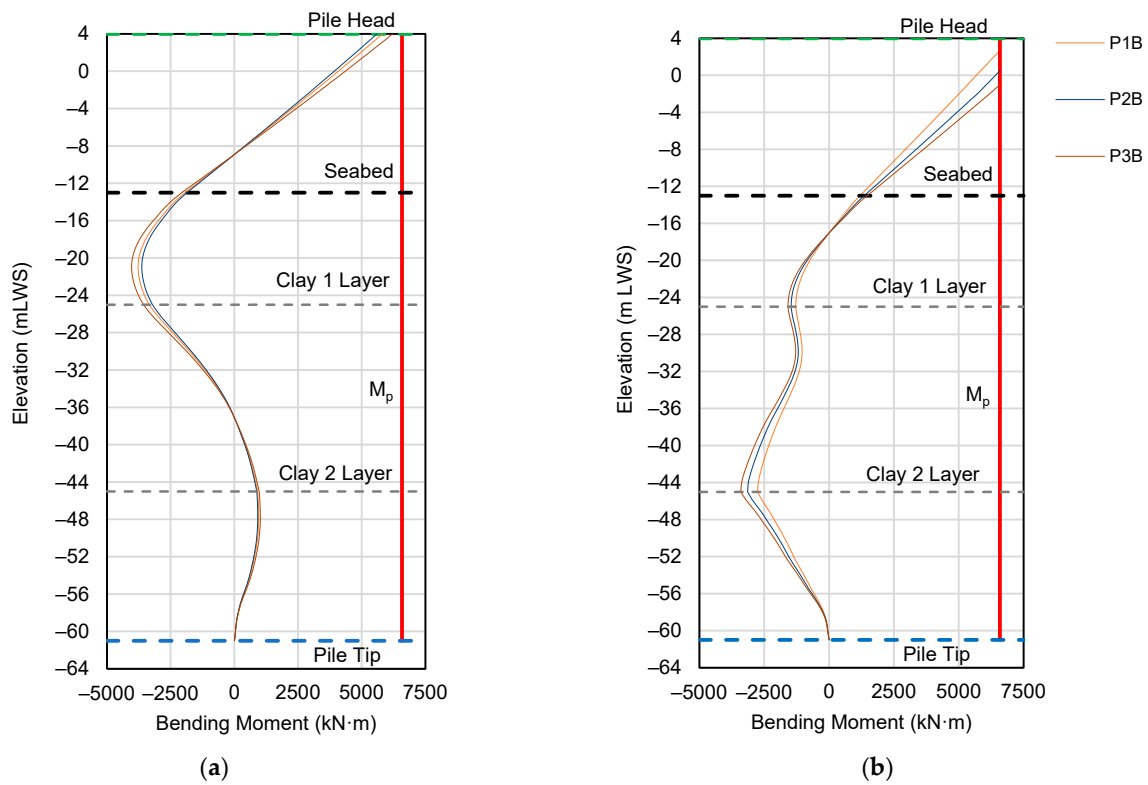


Figure 17. Bending moment distribution of Ø1200 mm pile due to the SDW. (a) Scenario 1; (b) Scenario 2.

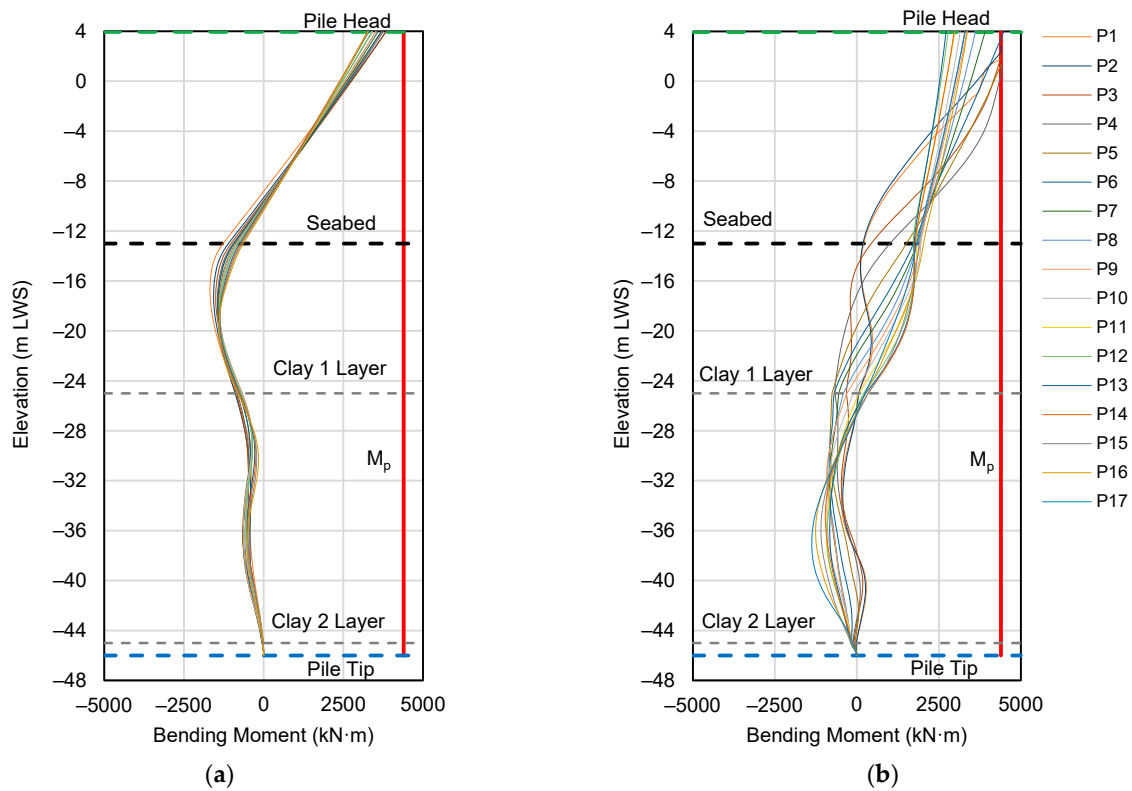


Figure 18. Bending moment distribution of Ø1000 mm pile due to the LDW. (a) Scenario 1; (b) Scenario 2.

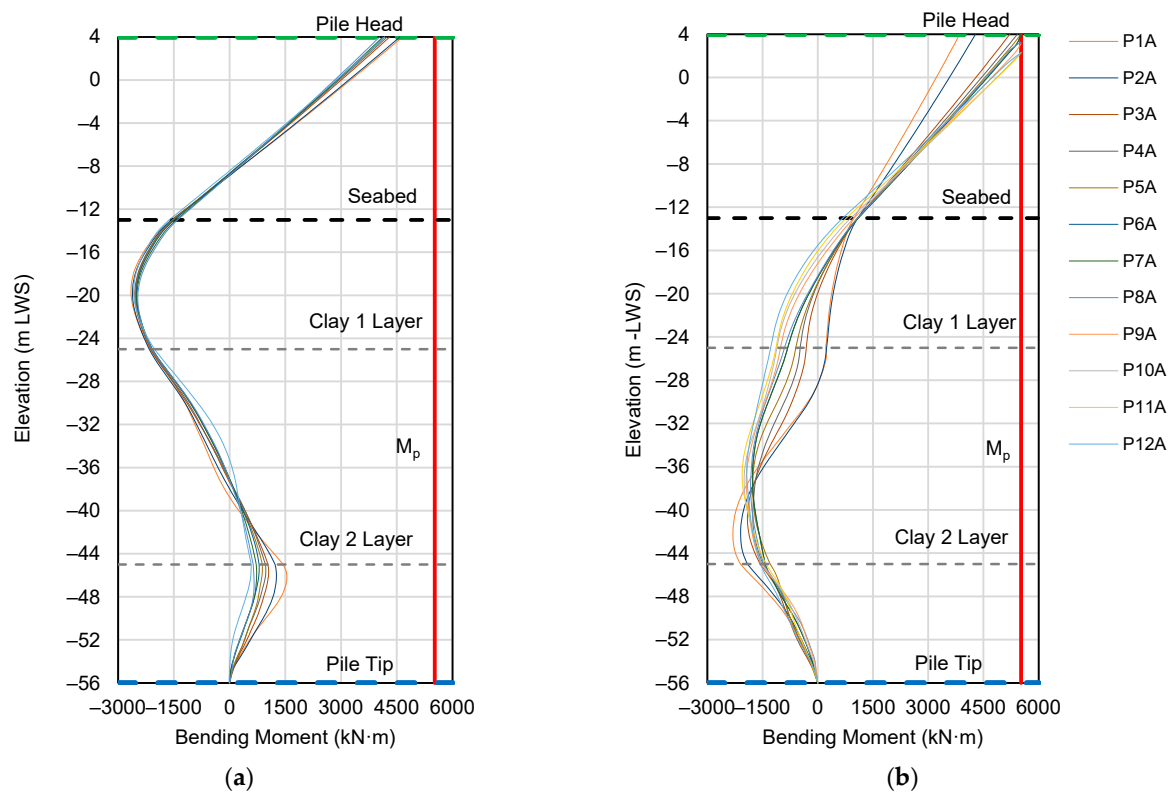


Figure 19. Bending moment distribution of Ø1100 mm pile due to the LDW. (a) Scenario 1; (b) Scenario 2.

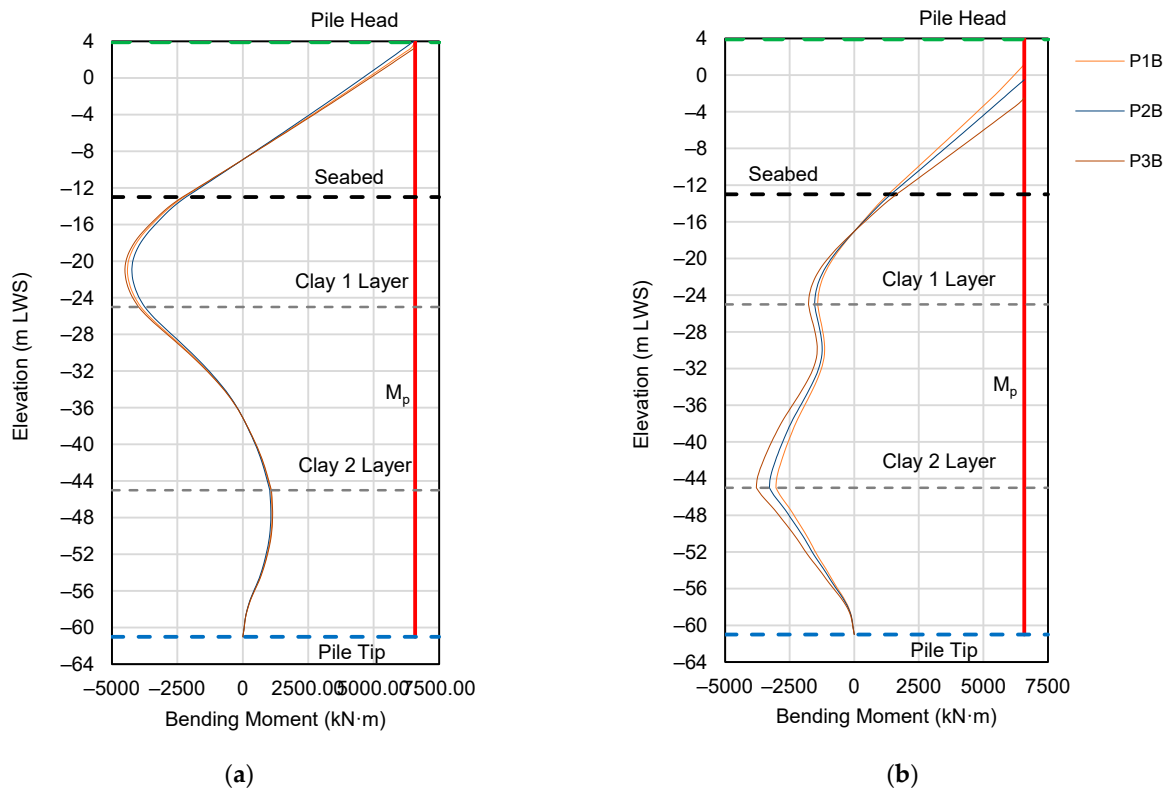


Figure 20. Bending moment distribution of Ø1200 mm pile due to the LDW. (a) Scenario 1; (b) Scenario 2.

In all the cases, the maximum bending moments were observed at pile heads. The maximum bending moments in the $\text{Ø}1200$ mm piles were significantly large. In Scenario 1, there was no pile that reached the plastic bending moment when the SDW was applied, but the plastic bending moment was reached in the $\text{Ø}1200$ mm pile when the LDW was applied. In Scenario 2, the plastic bending moments were reached at the $\text{Ø}1000$, $\text{Ø}1100$, and $\text{Ø}1200$ mm piles for any action of SDW and LDW. The reason why the bending moment of the $\text{Ø}1200$ mm pile was large in Scenario 1 is that the $\text{Ø}1200$ mm pile shared the largest inertia force because of its highest rigidity among the piles. In Scenario 2, in addition to the above, the $\text{Ø}1000$ mm piles were strongly affected by the ground displacement at the slope, resulting in a large bending moment, particularly in the piles close to the top of the slope.

Regarding the bending moment distribution below the ground surface, the results of Scenario 1 showed the maximum bending moment at shallow points in the underground. This bending moment profile is consistent with that generated in the beam on the Winkler foundation [41]. On the other hand, the results of Scenario 2 did not produce the maximum bending moment at shallow points in the ground. The explanation is that the ground stiffness and subgrade reaction were lowered in the shallow part of the ground due to the effect of the slope displacement. In contrast, large bending moments occurred at the boundary between Clay 2 and Clay 3 in Scenario 2 results. This is the same mechanism that caused buckling to occur at deep underground locations of the piles of the PSW at Kobe Port during the 1995 Kobe Earthquake because of the strong impedance contrast in soil layers [42]. Since the slope was gentle in the target wharf of this study, the plasticization of the pile did not occur in the underground part, but care should be taken that seismic design practice ignoring slope displacement may lead to the design results being on the dangerous side even for points in the underground.

Figures 21 and 22 illustrate the time histories of bending moments at the $\text{Ø}1200$ mm pile head due to the SDW and the LDW, respectively. The comparison between the bending moment time history of the piles and the acceleration and displacement time history of the PSW in Scenario 1 shows a correlation in amplitude patterns; large acceleration and displacement correspond to a large bending moment and vice versa. For example, for the SDW in Scenario 1, in the time range of 17–52 s, Figures 7a, 11a and 21a show large acceleration, displacement, and bending moment values, respectively. The largest value of pile bending moment, PSW acceleration, and displacement occurred simultaneously at 43 s. In addition, the smallest value coincided in the time range of 0–10 s. This correlation exists because the pile bending moments and displacement in Scenario 1 were significantly influenced by the inertial force of the structure. This pattern is also present in the LDW in Scenario 1.

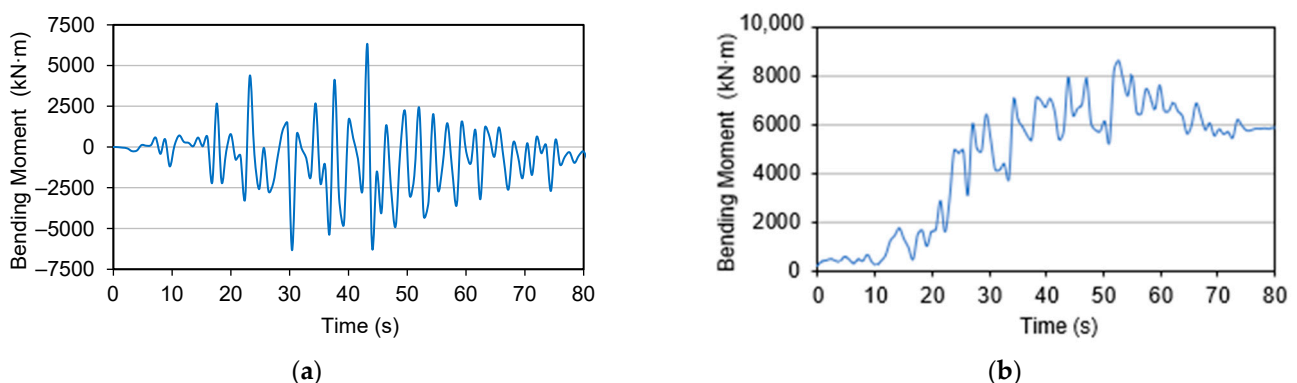


Figure 21. Bending moment time history of the pile due to the SDW. (a) Scenario 1; (b) Scenario 2.

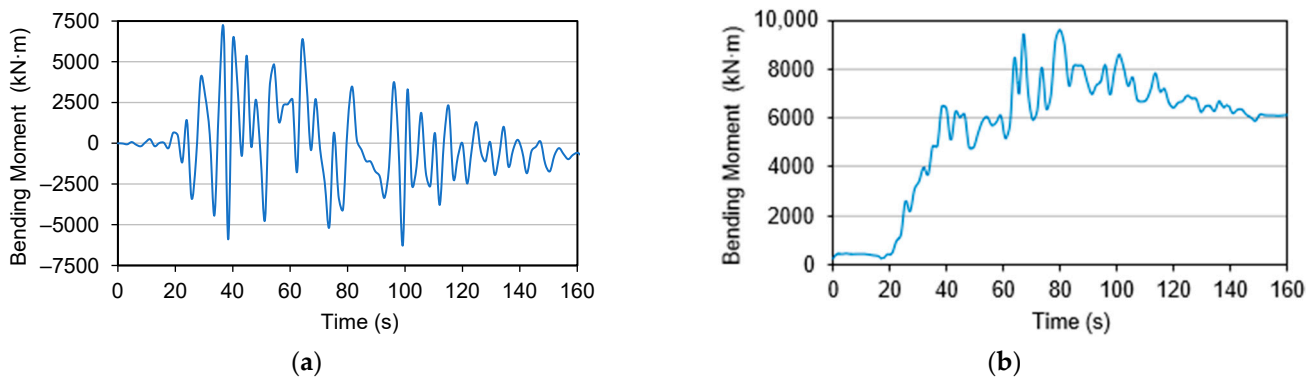


Figure 22. Bending moment time history of the pile due to the LDW. (a) Scenario 1; (b) Scenario 2.

A comparison between the bending moment time history of piles and the acceleration time history of PSW in Scenario 2 indicates that the bending moment was influenced not only by the inertial force of the structure but also by the displacement of the soil slope which was not considered in Scenario 1. Figure 21b shows that the bending moment in Scenario 2 was not zero at 0 s. The additional bending moment value is caused by the lateral displacement of the soil slope at the static phase (before the earthquakes). Figure 23 shows the horizontal residual ground displacement in the static phase. The maximum horizontal residual ground displacement in the static phase of Scenario 2 was 0.034 m (Figure 23b), far more significant than the 0.0007 m in Scenario 1 (Figure 23a). Thus, the effect of the soil displacement on the bending moment was more significant in Scenario 2.

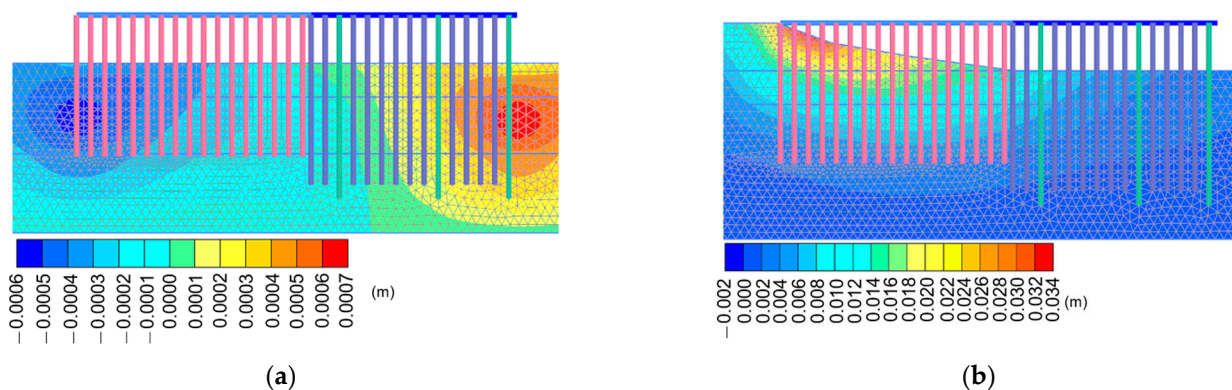


Figure 23. Horizontal residual ground displacement before earthquakes. (a) Scenario 1; (b) Scenario 2.

A comparison between the bending moment time history of piles at SDW in Scenario 1 and Scenario 2 also indicates the influence of the displacement at the soil slope in Scenario 2. At 53 s, the bending moment in Scenario 2 (Figure 21b), PSW acceleration (Figure 9a), and PSW displacement (Figure 11b) show values of 8630 kN·m, 0.35 g, and 1.1 m, respectively. Whereas, at 43 s, the bending moment in Scenario 1 (Figure 21a), PSW acceleration (Figure 7a), and PSW displacement (Figure 11a) show values of 6315 kN·m, 0.55 g, and 0.55 m, respectively. From those values, we can observe that the smaller acceleration in Scenario 2 (i.e., 0.35 g) could lead to the larger bending moment (i.e., 8630 kN·m) due to the influence of relatively larger displacement (i.e., 1.1 m).

A comparison between Figures 21a and 22a demonstrates that the waveform duration could influence the maximum bending moment value. For example, LDW in Scenario 1 produces a more significant maximum bending moment of 6950 kN·m (Figure 22a) than SDW of 6315 kN·m (Figure 21a). A similar difference is also present in Scenario 2. This difference is due to the different phase characteristics of the SDW and LDW used in this study, as depicted in Figures 8a and 10a, where the LDW produces larger PSW Fourier spectra than SDW at the natural period of PSW.

4. Conclusions

The PSW seismic design practice often neglects the effect of ground displacement at mild soil slope. Thus, only the framed structural element has been generally modeled. Our study used a 2D soil-structure system FEA to examine a wide PSW's seismic performance associated with soil-structure dynamic interaction. Additionally, two waveforms of different durations were employed as motion inputs to investigate the impact of seismic duration on the PSW's seismic response.

The main conclusions drawn from this study are as follows:

1. The 2D soil-structure system FEA provides a reliable tool for PSW's seismic performance assessment and is effective for taking into account the effect of ground displacement and waveform durations.
2. Seismic codes generally stipulate only SA as seismic load; however, various time history waveforms can be realized for the same SA. Different waveforms left significantly different maximum PSW displacement and bending moment of the pile. Therefore, various time-history waveforms should be considered when conducting seismic design while paying attention to the phase characteristics.
3. Different FEA modeling conditions (i.e., with/without considering the soil slope) resulted in different bending moments in the piles and residual displacements of PSWs. Even in cases of mild soil slope under the PSW, the effect of the ground displacement is significant. Therefore, ground displacement in soil slope should be given special attention in design practice.
4. Different FEA modeling conditions (i.e., with/without considering the soil slope) show different vibration characteristics of the PSWs. When considering the soil slope, the natural period of the PSW becomes shorter because the free length of the pile in the soil slope becomes shorter. Therefore, attention should be paid to determining the correct natural period of the PSW.
5. In the case where the soil slope is considered, a relatively significant bending moment occurs at the boundary between soil layers. Therefore, attention shall be paid to the comparatively sizeable bending moment generated in the boundary of soil layers with significant impedance contrast.

Author Contributions: Conceptualization, C.B. and T.N.; methodology, C.B. and T.N.; software, C.B.; validation, C.B. and T.N.; formal analysis, C.B. and T.N.; investigation, C.B. and T.N.; resources, C.B. and T.N.; data curation, C.B.; writing—original draft preparation, C.B.; writing—review and editing, T.N.; visualization, C.B.; supervision, T.N.; project administration, C.B.; funding acquisition, C.B. All authors have read and agreed to the published version of the manuscript.

Funding: This research was funded by PT. Inti Teknik Solusi Cemerlang (PT. ITSC), grant number: 036/ADM.ITSC/VIII/2019 and the APC were funded by PT. ITSC.

Institutional Review Board Statement: Not applicable.

Informed Consent Statement: Not applicable.

Data Availability Statement: The datasets generated during and/or analysed during the current study are available from the corresponding author on reasonable request.

Acknowledgments: The authors would like to express their gratitude to the PT. Inti Teknik Solusi Cemerlang (PT. ITSC) for providing PLAXIS 2D Software.

Conflicts of Interest: The authors declare no conflict of interest.

References

1. Kayen, R.E.; Mitchell, J.K.; Seed, R.B.; Nishio, S. Soil Liquefaction in the East Bay during the Earthquake. 1998. Available online: https://www.researchgate.net/publication/294571172_Soil_liquefaction_in_the_east_bay_during_the_earthquake/fullTextFileContent (accessed on 10 July 2022).

2. Werner, S.; McCullough, N.; Bruin, W.; Augustine, A.; Rix, G.; Crowder, B.; Tomblin, J. Seismic Performance of Port de Port-Au-Prince during the Haiti Earthquake and Post-Earthquake Restoration of Cargo Throughput. *Earthq. Spectra* **2011**, *27*, 387–410. [[CrossRef](#)]
3. Su, L.; Lu, J.; Elgamal, A.; Arulmoli, A.K. Seismic Performance of a Pile-Supported Wharf: Three-Dimensional Finite Element Simulation. *Soil Dyn. Earthq. Eng.* **2017**, *95*, 167–179. [[CrossRef](#)]
4. Heidary-Torkamani, H.; Bargi, K.; Amirabadi, R.; McCllough, N.J. Fragility Estimation and Sensitivity Analysis of an Idealized Pile-Supported Wharf with Batter Piles. *Soil Dyn. Earthq. Eng.* **2014**, *61–62*, 92–106. [[CrossRef](#)]
5. Hamrouni, A.; Deghoul, L.; Gabi, S. The Influence of the Soil Constitutive Models on the Seismic Analysis of Pile-Supported Wharf Structures with Batter Piles in Cut-Slope Rock Dike. *Stud. Geotech. Mech.* **2020**, *42*, 191–209. [[CrossRef](#)]
6. Nagao, T.; Lu, P. A Simplified Reliability Estimation Method for Pile-Supported Wharf on the Residual Displacement by Earthquake. *Soil Dyn. Earthq. Eng.* **2020**, *129*, 105904. [[CrossRef](#)]
7. Du, J.; Wang, H.; Wang, S.; Song, X.; Wang, J.; Chang, A. Fatigue Damage Assessment of Mooring Lines under the Effect of Wave Climate Change and Marine Corrosion. *Ocean Eng.* **2020**, *206*, 107303. [[CrossRef](#)]
8. Martinez, M.J. Harbor And Coastal Structures: A Review Of Mechanical Fatigue Under Random Wave Loading. *Heliyon* **2021**, *7*, e08241. [[CrossRef](#)]
9. Liang, Q.; Zhao, C.; Hu, J.; Zeng, H. An Analytical Method for Elastic Seismic Response of Structures Considering the Effect of Ground Motion Duration. *Appl. Sci* **2021**, *2021*, 10949. [[CrossRef](#)]
10. Dobry, R.I.; Idriss, M.; Ng, E. Duration Characteristics of Horizontal Components of Strong-Motion Earthquake Records. *Bull. Seismol. Soc. Am.* **1978**, *68*, 1487–1520.
11. Shoji, Y.; Tanii, K.; Kamiyama, M. A Study on the Duration and Amplitude Characteristics of Earthquake Ground Motions. *Soil Dyn. Earthq. Eng.* **2005**, *25*, 505–512. [[CrossRef](#)]
12. Barbosa, A.R.; Ribeiro, F.L.A.; Neves, L.C. Effects of Ground-Motion Duration on the Response of a 9-Story Steel Frame Building. In Proceedings of the 10th U.S. National Conference on Earthquake Engineering, Anchorage, AK, USA, 21–25 July 2014.
13. Ou, Y.-C.; Song, J.; Wang, P.-H.; Adidharma, L.; Chang, K.-C.; Lee, G.C. Ground Motion Duration Effects on Hysteretic Behavior of Reinforced Concrete Bridge Columns. *J. Struct. Eng.* **2014**, *140*, 04013065. [[CrossRef](#)]
14. Romney, K.T.; Barbosa, A.R.; Mason, H.B. Developing a Soil Bridge-Interaction Model for Studying the Effects of Long-Duration Earthquake Motions. In Proceedings of the 10th U.S. National Conference on Earthquake Engineering, Anchorage, AK, USA, 21–25 July 2014.
15. Mantawy, A.; Anderson, J.C. Effect of Long-Duration Earthquakes on the Low-Cycle Fatigue Damage in RC Frame Buildings. *Soil Dyn. Earthq. Eng.* **2018**, *109*, 46–57. [[CrossRef](#)]
16. Chandramohan, R. Duration of Earthquake Ground Motion: Influence on Structural Collapse Risk And Integration in Design and Assessment Practice. Ph.D. Thesis, Stanford University, Stanford, CA, USA, August 2016.
17. Chiou, J.S.; Chiang, C.H.; Yang, H.H.; Hsu, S.Y. Developing Fragility Curves for a Pile-Supported Wharf. *Soil Dyn. Earthq. Eng.* **2011**, *31*, 830–840. [[CrossRef](#)]
18. Zacchei, E.; Lyra, P.H.C.; Stucchi, F.R. Nonlinear Static Analysis of a Pile-Supported Wharf. *Rev. IBRACON Estruturas e Mater.* **2019**, *12*, 998–1009. [[CrossRef](#)]
19. Zacchei, E.; Lyra, P.H.C.; Stucchi, F.R. Pushover Analysis for Flexible and Semi-Flexible Pile-Supported Wharf Structures Accounting the Dynamic Magnification Factors Due to Torsional Effects. *Struct. Concr.* **2020**, *21*, 2669–2688. [[CrossRef](#)]
20. Chen, Y.; Sun, H.; Feng, Z.; Chen, Y.; Sun, H.; Feng, Z. Study on Seismic Isolation of Long Span Double Deck Steel Truss Continuous Girder Bridge. *Appl. Sci.* **2022**, *12*, 2567. [[CrossRef](#)]
21. Stehmeyer, E.H. Seismic Vulnerability Assessments of Marine Structures Using Non-Linear Static Analysis Procedures. In Proceedings of the Structures Congress 2011, Las Vegas, NV, USA, 14–16 April 2011; pp. 2297–2308. [[CrossRef](#)]
22. Widyastuti, H.; Lumantarna, E.; Sofi, M.; Ramli, M.I.; Oktavianus, Y.; Rajabifard, A. Earthquake Vulnerability of Port Structures in Indonesia. *IOP Conf. Ser. Earth Environ. Sci.* **2020**, *419*, 012001. [[CrossRef](#)]
23. Imai, T.; Tonouchi, K. Correlation of N Value with S-Wave Velocity and Shear Modulus. In Proceedings of the 2nd European Symposium on Penetration Testing, Amsterdam, The Netherlands, 24–27 May 1982; Routledge: Amsterdam, The Netherlands, 1982; pp. 67–72.
24. SNI 1726:2019; Tata Cara Perencanaan Ketahanan Gempa Untuk Struktur Bangunan Gedung Dan Non Gedung. BSN: Jakarta, Indonesia, 2019.
25. PLAXIS Company (Plaxis B.V.). *PLAXIS CONNECT Edition V21.00 General Information Manual*; Plaxis B.V.: Delft, The Netherlands, 2021.
26. Toma, M.A. Earthquake Response Analysis of Pile Supported Structures. Master’s Thesis, Norwegian University of Science and Technology, Trondheim, Norway, June 2017.
27. PLAXIS Company (Plaxis B.V.). *PLAXIS CONNECT Edition V21.00 Material Models Manual*; Plaxis B.V.: Delft, The Netherlands, 2021.
28. Dao, T.P.T. Validation of PLAXIS Embedded Piles for Lateral Loading. Master of Science Thesis, Delft University of Technology, Delft, The Netherlands, April 2011.
29. van der Kwaak, B. Modelling of Dynamic Pile Behaviour during an Earthquake Using PLAXIS 2D: Embedded Beam (Row). Master of Science Thesis, Delft University of Technology, Delft, The Netherlands, December 2015.

30. Sluis, J.; Besseling, F.; Stuurwold, P.; Lengkeek, A. Validation and Application of the Embedded Pile Row Feature in PLAXIS 2D. *Plaxis Bull.* **2013**, *34*, 10–13.
31. Bowles, J.E. *Physical and Geotechnical Properties of Soils*; McGraw-Hill Education: New York, NY, USA, 1984; ISBN 0070661944.
32. Obaji, N.O.; Komolafe, O.O.; Oke, J.A. Prediction of Initial Void Ratio from the Natural Moisture Content of Cohesive Soils. *Unibuja J. Eng. Technol.* **2020**, *1*, 1–13.
33. Benz, T. Small-Strain Stiffness of Soils and Its Numerical Consequences. Doctor of Engineering Thesis, Universität Stuttgart, Stuttgart, Germany, March 2007.
34. Broms, B.B. Lateral Resistance of Piles in Cohesive Soils. *J. Soil Mech. Found. Div.* **1964**, *90*, 27–63. [[CrossRef](#)]
35. Décourt, L. Prediction of the Bearing Capacity of Piles Based Exclusively on N Values of the SPT. In *Penetration Testing*; Routledge: London, UK, 1982; p. 6. ISBN 9780203743959.
36. Décourt, L.; Quaresma, A. Capacidade de Carga de Estacas a Partir de Valores de SPT. *Congr. Bras. Mecânica dos Solos e Eng. Fundações* **1978**, *1*, 45–53.
37. Boyke, C.; Refani, A.N.; Nagao, T. Site-Specific Earthquake Ground Motions for Seismic Design of Port Facilities in Indonesia. *Appl. Sci.* **2022**, *12*, 1963. [[CrossRef](#)]
38. Nagao, T. Maximum Credible Earthquake Ground Motions with Focus on Site Amplification Due to Deep Subsurface. *Eng. Technol. Appl. Sci. Res.* **2021**, *11*, 6873–6881. [[CrossRef](#)]
39. Vucetic, M.; Dobry, R. Effect of Soil Plasticity on Cyclic Response. *J. Geotech Eng.* **1991**, *117*, 89–107. [[CrossRef](#)]
40. Boore, D.M. *TSPP, a Collection of FORTRAN Programs for Processing and Manipulating Time Series*; U.S. Geological Survey Open-File Report 2008-1111; U.S. Geological Survey: Reston, VA, USA, 2009.
41. Hirai, H. A Winkler Model Approach for Vertically and Laterally Loaded Piles in Nonhomogeneous Soil. *Int. J. Numer. Anal. Methods Geomech.* **2012**, *36*, 1869–1897. [[CrossRef](#)]
42. Tokimatsu, K.; Asaka, Y. Effects Of Liquefaction-Induced Ground Displacements On Pile Performance In The 1995 Hyogoken-Nambu Earthquake. *Soils Found.* **1998**, *38*, 163–177. [[CrossRef](#)]